nature climate change

Article

https://doi.org/10.1038/s41558-026-02633-w

Increasing tropical cyclone rainfall and landslide risk in Southern California

Received: 5 May 2025

Accepted: 9 April 2026

Laiyin Zhu[1], **Yuan Wang**[2] ✉, **Kerry Emanuel**[3], **Sasha N. Tolstoff**[2] & **Noah S. Diffenbaugh**[2,4]

Tropical cyclone (TC) risk has long been overlooked in Southern California due to its relatively low historical frequency. Here we couple a physics-based TC downscaling model with a probabilistic, machine learning-based landslide model to assess changes in TC rainfall and landslide risks in ten Southern California counties. Historical simulations and reanalysis data show robust agreement in downscaled TC rainfall. The return period of Hurricane-Hilary-magnitude rainfall (~100 mm) shortens by 50% from 110 years to 54 years in a future high-emission warming scenario. Eastern Pacific sea surface temperature is projected to increase by 2.7 ± 0.7 °C from 1985–2014 to 2071–2100 and, together with enhanced mid-tropopsheric moisture, contribute to increasing TC rainfall risk. All Southern California counties exhibit growth in areas exposed to landslides from 2000 to 2050. The steepest fractional increases in landslide exposure exist in low-income households with a heavy tax burden. These findings underscore a pressing need for proactive and equitable planning and mitigation strategies for TC rainfall-induced hazards.

Tropical cyclones (TCs) cause massive amounts of damage globally[1–3]. In the USA, damage caused by TCs occurs primarily along the Atlantic and Gulf coasts[4,5]. In comparison, the Pacific coast of the USA is less exposed to landfalling TCs due to lower local sea surface temperatures (SSTs) driven by cold currents and upwelling in the eastern Pacific Ocean[6]. Historically, strong TCs have occasionally made landfall in Southern California, causing catastrophic damage[7]. For example, the 1939 California tropical storm cost 43 dead or missing and US$1 million damages (US$22.6 million today with inflation adjustment)[8]. In 2023, Hurricane Hilary produced massive inland flooding and landslides in Southern California and the Baja California peninsula in Mexico, resulting in three fatalities and over US$900 million in damages[9].

Historically, Southern California has frequently observed landslide cases with fatalities (Supplementary Fig. 1). Previous literature has also discussed the major contribution of atmospheric rivers to California's wet season precipitation and their ability to generate an extreme 'mega flood' event[10]. During summer and fall seasons, TCs can produce more intense rain rates within a short period than atmospheric rivers[11], and trigger severe flash floods and landslides[9,12]. For example, Hurricane Hilary (Supplementary Fig. 2a) has produced record daily rainfall in Los Angeles (63 mm) and San Diego (46 mm) since 1877 and 1875, respectively[9]. Moreover, landfalling TCs during Southern California's warm and dry season have the potential to compound with drought and wildfires, creating 'whiplash' storms[13] with unique associated risks.

A heavy TC rainfall event in this region is normally described as a 'grey swan' event—a high-impact event that cannot be precisely predicted by historical data but can be anticipated based on available physical knowledge of the climate system[14]. Recent climate change has established regional oceanic and atmospheric conditions that increasingly favour the development of such 'grey swan' TC events, including the rapidly rising ocean surface temperature along the California coast[15], greater atmospheric instability[16] and enhanced atmospheric moisture capacity following the Clausius–Clapeyron scaling[17,18].

---

[1]School of Environment, Geography and Sustainability, Western Michigan University, Kalamazoo, MI, USA. [2]Department of Earth System Science, Stanford University, Stanford, CA, USA. [3]Department of Earth, Atmospheric and Planetary Sciences, Massachusetts Institute of Technology, Cambridge, MA, USA. [4]Woods Institute for the Environment, Stanford University, Stanford, CA, USA. ✉e-mail: yzwang@stanford.edu

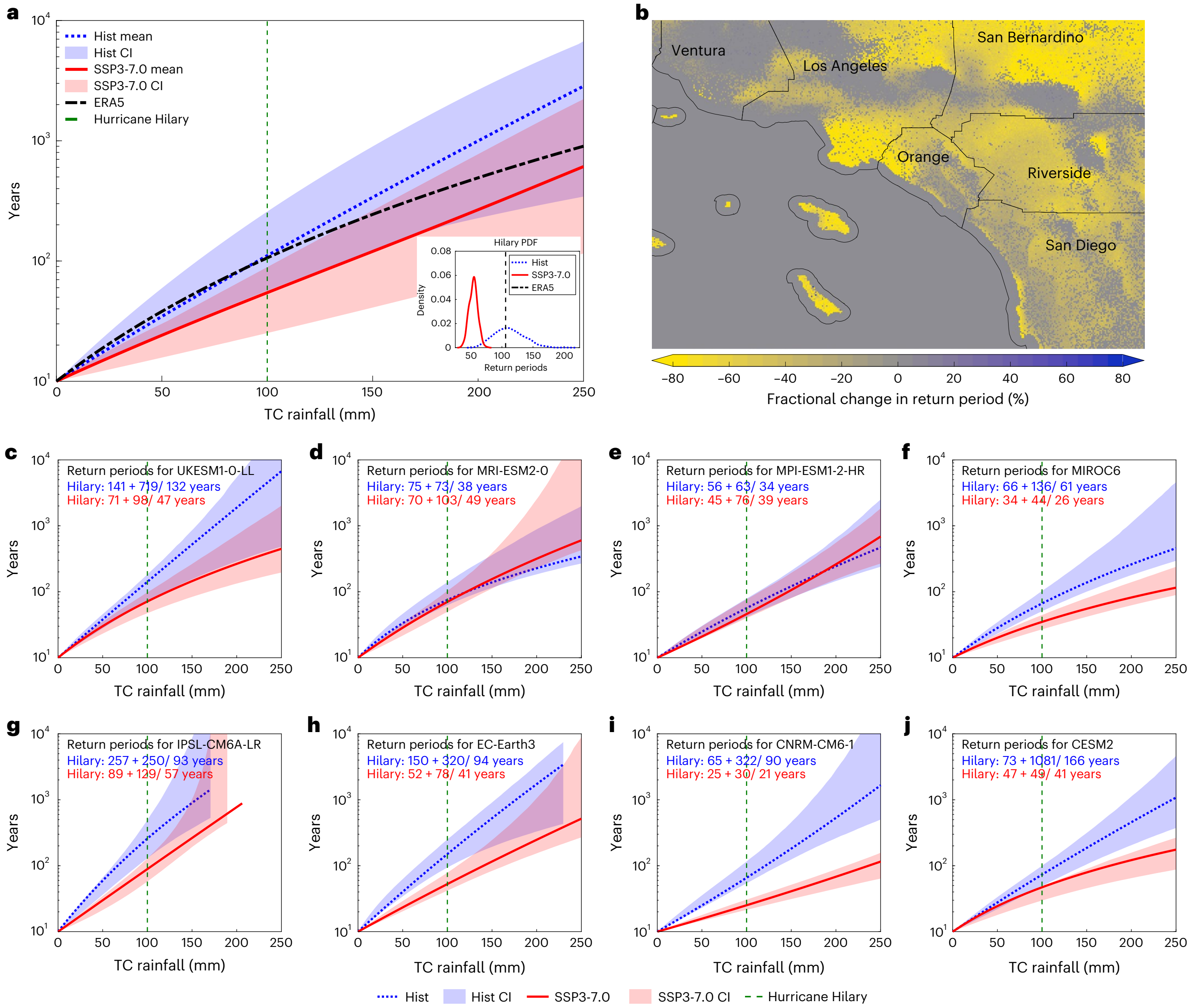

Fig. 1 | TC rainfall and its return periods based on the historical and SSP3-7.0 climate scenarios. a, Multi-model mean of TC rainfall return period. Lines represent eight model ensemble means for the historical (Hist) runs (blue), SSP3-7.0 runs (red) and the ERA5 run (black) for Los Angeles (34° 03′ N, 118° 15′ W), and shadings represent upper and lower model estimates from the historical ensemble (blue) and SSP3-7.0 ensemble (red). Inset shows the probability distribution functions (PDF) for return periods (years) of 100-mm TC rainfall based on eight models of historical and SSP3-7.0 climate scenarios, estimated by bootstrapping ensemble GCM estimates. **b**, Fractional changes in return periods of the 100 mm TC rainfall between the historical ensemble mean and the SSP3-7.0 ensemble mean at all locations (formula shown in the panel). **c**–**j**, Lines show the mean TC rainfall risk for Los Angeles, estimated from downscaling eight climate models (UKESM1-0-LL (**c**), MRI-ESM2-0 (**d**), MPI-ESM1-2-HR (**e**), MIROC6 (**f**), IPSL-CM6A-LR (**g**), EC-Earth3 (**h**), CNRM-CM6-1 (**i**) and CESM2 (**j**)), for the historical (blue) and SSP3-7.0 (red) runs. Shadings are 95% confidence intervals (CIs) calculated from 1,000 bootstrap samples for each of the 100 steps, based on the Monte Carlo algorithm that fits each GPD (Methods). Green dashed lines in panels **a** and **c**–**j** represent Hurricane Hilary's accumulative precipitation (~100 mm) for Los Angeles. The return periods of 100 mm TC rainfall and 95% CIs are also labelled for Hist runs (blue) and SSP3-7.0 runs (red) in panels **c**–**j**. Basemap in **b** created with MATLAB[28].

Such heavy TC rainfall events pose a particular risk for Southern California, home to major metropolitan areas like Los Angeles and San Diego, the 2nd and 23rd largest urban areas in the USA, according to the 2023 census data[19]. Groups with diverse socioeconomic statuses reside in this region, potentially creating social disparities in exposure to weather-related disasters and in certain communities' ability to recover from extreme weather events. Moreover, complex regional orography is known to strengthen precipitation over the mountain ranges[14,20,21] and create vulnerable environments for severe landslides[22,23].

Despite these risks, there is still limited knowledge about the specific risks of 'grey swan' TC events in Southern California. Previous work has discussed the connections between landslide risk and rainfall variabilities under the present and future climate[24–27]. Still, our understanding of TC rainfall's role in landslides is constrained by limited historical observation records, particularly for Southern California. Given those gaps, we integrate a physics-based synthetic TC model with a machine learning-based probabilistic landslide model and high-resolution population information to investigate how global warming influences the probability of TC rainfall in Southern California, what the possible controlling factors are, how changes in TC rainfall risk influence landslide risk and whether social disparities exist in exposure to the changing TC rainfall-induced landslide risk.

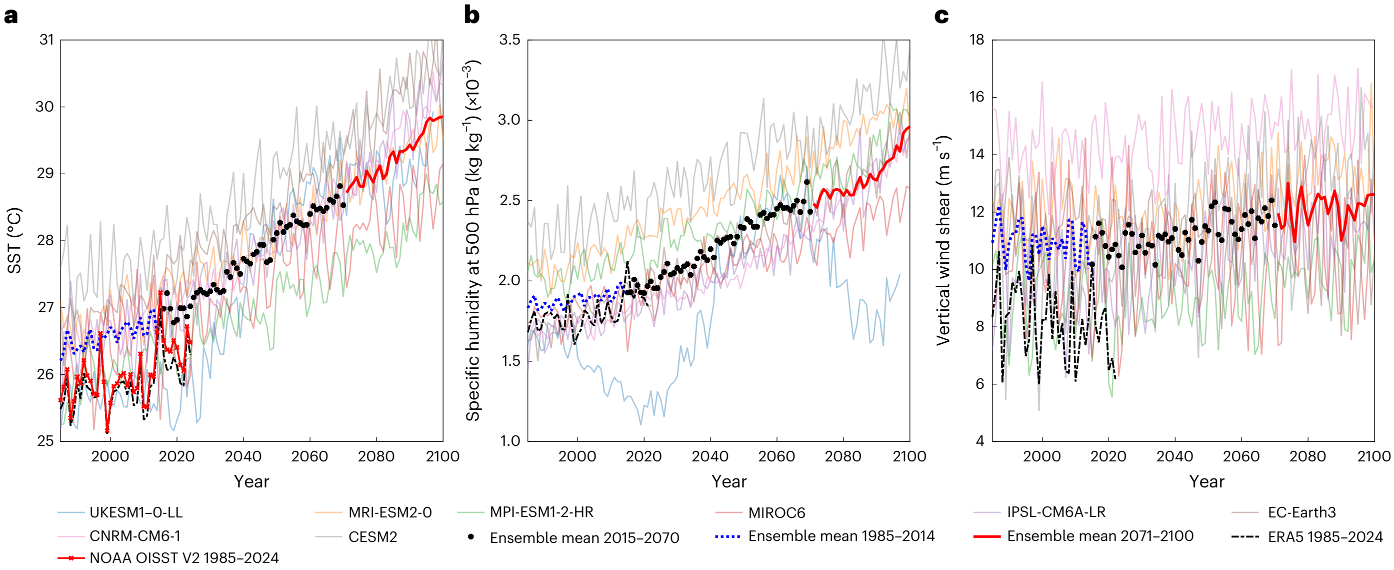

Fig. 2 | Evolutions of environmental variables relevant to TC dynamics and rainfall. a, SSTs from eight CMIP6 GCM models UKESM1-0-LL, MRI-ESM2-0, MPI-ESM1-2-HR, MIROC6, IPSL-CM6A-LR, EC-Earth3, CNRM-CM6-1 and CESM2, their ensemble means, ERA5 reanalysis and the National Oceanic and Atmospheric Administration Optimum Interpolation Sea Surface Temperature V2 dataset. **b**, Specific humidity at 500 hPa for eight CMIP6 GCM models and the ERA5 reanalysis. **c**, Vertical wind shear calculated between 200 hPa and 850 hPa for eight CMIP6 GCM models and the ERA5 reanalysis. All metrics are based on seasonal means from May to November in the eastern Pacific TC development region from 1985 to 2100.

Elevated TC rainfall risk

We employ a physics-based TC rainfall model embedded in a synthetic TC downscaling framework (Methods and Supplementary Information) to predict rainfall spatial distributions at the event level. We filter 1,200 synthetic TCs within 500 km of Los Angeles (34.05° N, −118.24° W), downscaled from each of the eight global climate models (GCMs) in Phase 6 of the Coupled Model Intercomparison Project (CMIP6). The CMIP6 simulations include historical and Shared Socioeconomic Pathway (SSP) 3-7.0 future forcing scenarios[28,29]. The SSP3-7.0 scenario reflects a GHG pathway[30] with continued high levels of aerosol emissions and decreases in forest area, providing a more recommended GHG emission range for the impact assessment of future warming climate[31]. For comparison with historical climate variability, we also generate a synthetic TC set based on the European Centre for Medium-Range Weather Forecasts Reanalysis version 5 (ERA5) data. We then apply the generalized Pareto distribution (GPD) to model the tail of the heavy TC rainfall distribution (>90th percentile of the data, ~10 mm) and the return period curves (Methods). Multiple statistical tests (Supplementary Figs. 3–6 and Supplementary Table 2) demonstrate that the GPD technique has reasonable skills.

The ensemble means of all eight downscaled TC sets demonstrate systematically increased TC rainfall risk at Los Angeles and surrounding locations in response to global warming (Fig. 1a,b). The TC rainfall risk from ERA5 is generally consistent with the historical ensemble when the rainfall amount is less than 100 mm for the Hurricane Hilary event (Supplementary Fig. 2). The return period of the 100 mm TC rainfall event decreases by 50% (with uncertainty bounds between 19% and 77%), from ~110 years in both ERA5 and the historical simulations (bounds between 56 and 258 years) to 54 years in the SSP3-7.0 scenario (bounds between 25 and 89 years). The elevated TC rainfall risk is widespread in Southern California, with 144,157 km^2 (76%) of the study area exhibiting a greater than 50% reduction in the return period of the 100 mm TC rainfall (Fig. 1b). The total areas with <100 years of return period for the 100 mm TC rainfall increase from 12,004 km^2 (7.42%, Extended Data Fig. 1a) based on the historical ensemble mean estimate to 27,423 km^2 (15.4%, Extended Data Fig. 1b) based on the SSP3-7.0 estimate. Generally, heavier rainfall events associated with TCs are predicted to occur more frequently along the Southern California coast.

TC rainfall downscaled from eight individual CMIP6 GCMs (Fig. 1c–j) exhibits substantial inter-model variability in magnitude. Models UKESM1-0-LL, MIROC6, IPSL-CM6A-LR, EC-Earth3, CNRM-CM6-1 and CESM2 (Fig. 1c,f–j) show consistently larger increases in TC rainfall risk, whereas MRI-ESM2-0 and MPI-ESM1-2-HR (Fig. 1d,e) demonstrate minimal differences. MPI-ESM1-2-HR, MIROC6, CNRM-CM6-1 and CESM2 systematically estimate higher TC rainfall risk than the other GCMs, with return periods for the 100 mm event falling below 100 years in the SSP3-7.0 scenarios. EC-Earth3 and CNRM-CM6-1 (Fig. 1h,i) show larger fractional increases in TC rainfall risk, projecting six- to eight-fold greater TC rainfall under SSP3-7.0 than in historical simulations.

The GCM ensemble mean SST of the eastern Pacific Ocean TC development region (−80° W to −140° W and 5° N to 40° N) is projected to increase from 26.7 ± 0.6 °C in the historical period (1985–2014) to 29.3 ± 0.7 °C in SSP3-7.0 (2071–2100), with a slope of 0.03 °C per year ($P < 0.01$) from 1985 to 2100 (Fig. 2a and Extended Data Fig. 2). This increasing trend is consistent among the eight GCMs (Supplementary Fig. 7). We also independently identify warming trends (Fig. 2a) in historical SST observations from the ERA5 reanalysis (0.007 °C per year from 1940 to 2024, $P < 0.01$) and the National Oceanic and Atmospheric Administration Optimum Interpolation Sea Surface Temperature V2 dataset (0.016 °C per year from 1981 to 2024, $P < 0.01$). The regions with warmer SST (for example, above 26.5 °C) have expanded substantially northward (Extended Data Fig. 2). The absolute SST values show widespread increases from the historical simulations to SSP3-7.0 (Supplementary Fig. 8a). In contrast, the fractional increases are notably more pronounced in the northern region near the California coast (Supplementary Fig. 8b). All GCMs exhibit similar spatial patterns of SST warming, albeit with varying magnitudes of change (Supplementary Figs. 9–12). The GCMs showing larger increases of TC rainfall risk (UKESM1-0-LL, MIROC6, IPSL-CM6A-LR, EC-Earth3, CNRM-CM6-1 and CESM2, Fig. 1) also generally demonstrate larger increases in SST (Supplementary Fig. 11a,e–g). However, TC rainfall from different GCMs exhibit variability in their sensitivity to SST change (Extended Data Fig. 3a). Global and regional SSTs directly control rain rate following Clausius–Clapeyron scaling[32]. Our result

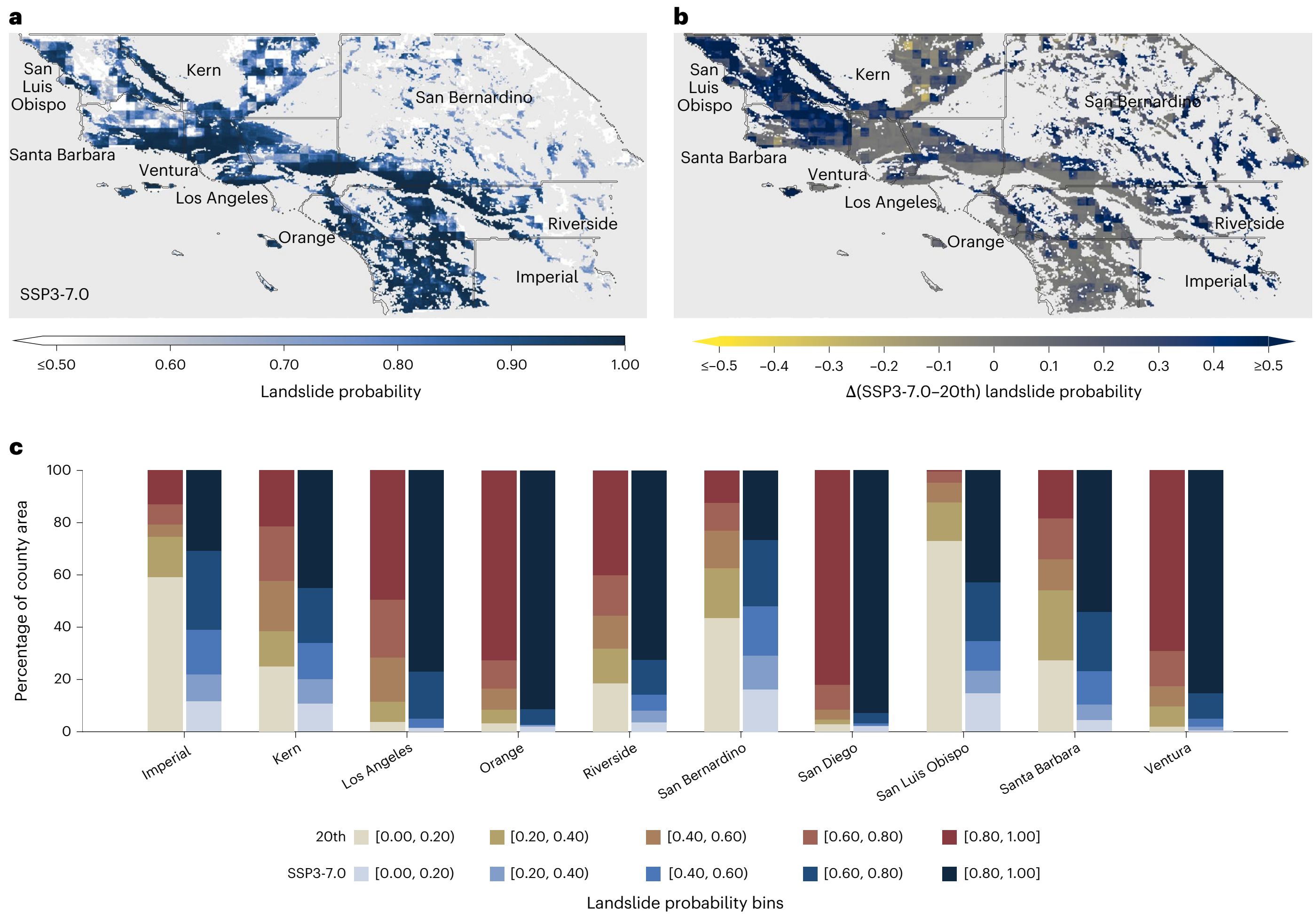

Fig. 3 | Landslide probability based on TC rainfall events with a 100-year return period. The maximum landslide probability is calculated across the three consecutive, most rainfall-intensive days for eight GCMs with 20 TC events each. **a**, Median landslide probability from the SSP3-7.0 ensemble. **b**, Changes in landslide probability from the historical ensemble to the SSP3-7.0 ensemble (calculated as SSP3-7.0 − historical). **c**, Fraction of areas with landslide probability from the historical ensemble median (blue) and the SSP3-7.0 ensemble median (red), summarized within different counties. Basemap administrative boundaries in **a** and **b** from GADM v.3.6.

indicates that the ensemble mean hourly TC rain rate with a 100-year return period is likely to increase by 28% from the historical to the SSP370 simulations (Extended Data Fig. 4). From our estimates, Clausius–Clapeyron scaling is ~9% per kelvin of SST change—larger than the theoretical value (7%) and the value (5%) reported by idealized climate model simulations[32].

Elevated atmospheric moisture increases TC rainfall risk in Southern California. Mid-level humidity is an important contributor to TC development, intensification and rainfall processes[33]. We observe a substantially increasing trend in the ensemble mean of specific humidity at 500 hPa in the eastern Pacific, with a slope of 9.2×10^{-6} kg kg^{-1}yr^{-1} ($P < 0.01$, Fig. 2b) from 1985 to 2100. The ERA5 reanalysis also shows an increasing trend in the specific humidity, with a slope of 4.2×10^{-6} kg kg^{-1}yr^{-1} from 1979 to 2024 ($P < 0.01$, Fig. 2b). The sensitivity varies across different GCMs for changes in TC risk to elevated specific humidity (Extended Data Fig. 3b). The GCM ensemble mean of eastern Pacific mid-level relative humidity also increases by 0.02% per year from 1985 to 2100, with ERA5 increasing by 0.045% per year from 1979 to 2024 (Supplementary Fig. 13).

In contrast, stronger vertical wind shear usually inhibits TC development[34,35] and could introduce asymmetries in TC rainbands[36,37]. We find an increasing trend in eastern Pacific vertical wind shear of between 200 hPa and 850 hPa, with a slope of 0.014 m s^{-1}yr^{-1} ($P < 0.01$) from 1985 to 2100 based on the GCM ensemble mean (Fig. 2c). Interestingly, ERA5 shows a statistically decreasing trend in vertical shear from 1979 to 2024, with a slope of −0.034 m s^{-1}yr^{-1} ($P = 0.03$).

Change in TC rainfall-induced landslides

Intense TC rainfall will destabilize the soil and likely create landslides on the mountain slopes[12]. Here we use the National Aeronautics and Space Administration Landslide Hazard Assessment for Situation Awareness model version 2.1 (LHASA 2.1)[38] to calculate local landslide probabilities (1-km grid) based on TC rainfall with the same initial soil moisture condition as Hurricane Hilary (Methods). We show that, on average, 79.5% (58,493.6 km^2) of Southern California is exposed to high landslide probability ($P > 0.5$) if hit by TC rainfall with a 100-year return period in SSP3-7.0 (Fig. 3a). Mountain ranges facing the Pacific Ocean (Supplementary Fig. 14) exhibit a larger landslide probability (Fig. 3a) and they show larger fractional changes than the inland region (Fig. 3b). The high landslide probability area ($P > 0.5$) increases by 20,847 km^2 (Fig. 3b), accounting for more than 55.4% of the historical scenario estimate (Supplementary Fig. 15).

All ten counties of interest exhibit an increased fraction of area exposed to higher landslide risk (Fig. 3c). Notably, as the most populous county, Los Angeles has 2,989 km^2 (49.6%) of its domain area exposed to severe landslide risk ($P > 0.8$) in the historical scenario. This severe risk area increases by 1,655.7 km^2 (+55.4%) in the SSP3-7.0 scenario, reaching 77.1% of Los Angeles' total area. Other densely

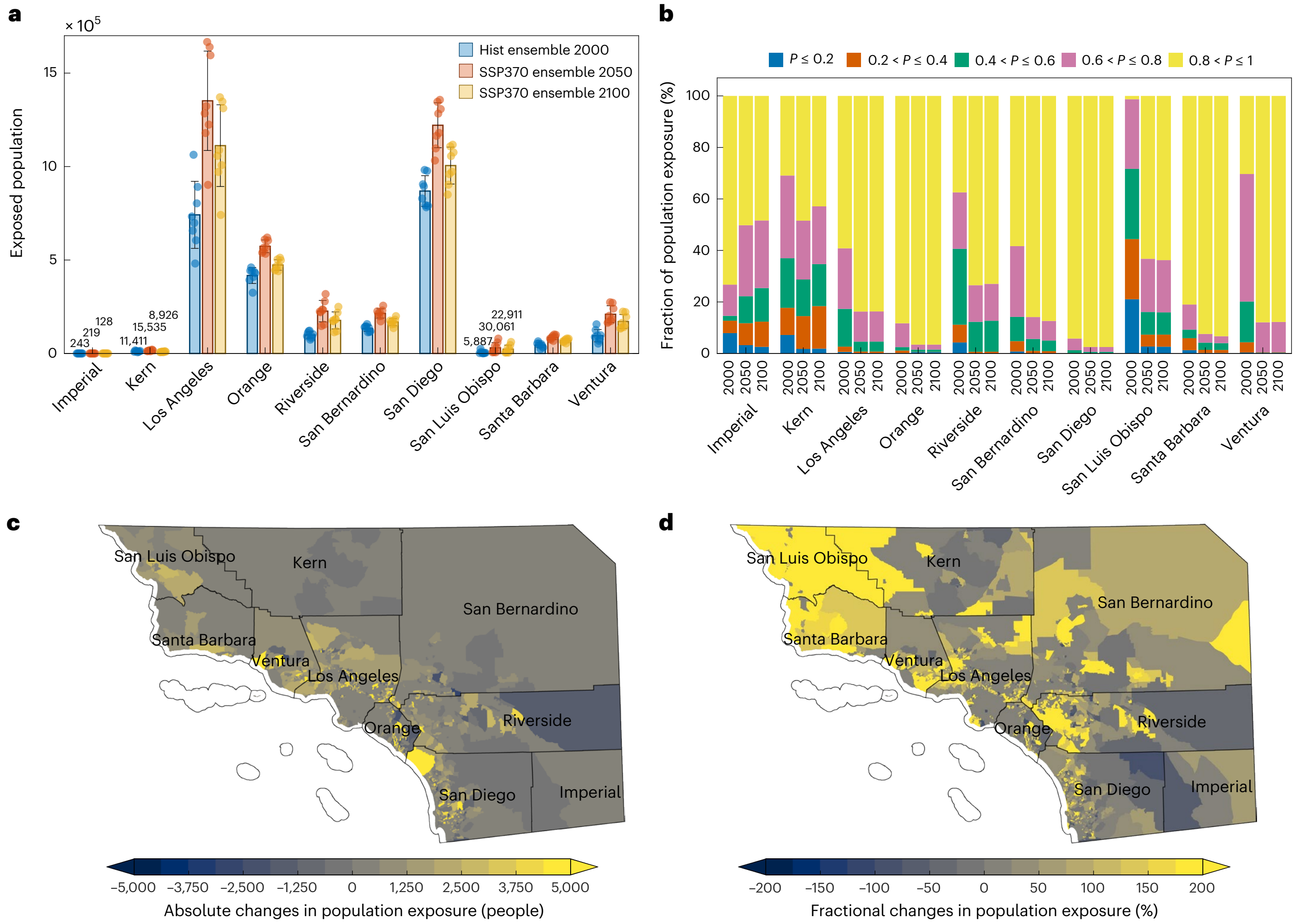

Fig. 4 | Changes in population exposure to landslides induced by TC rainfall events with a 100-year return period. a, Populations exposed to landslides in different counties. Eight GCM ensemble means are calculated as bars for the historical (Hist) ensemble + SSP3 population in 2000 (blue), SSP3-7.0 ensemble + SSP3 population in 2050 (red) and SSP3-7.0 ensemble + SSP3 population in 2100 (yellow), with error bars representing the standard deviations from eight GCM ensemble members in dots; ensemble means for Imperial, Kern and San Luis Obispo are labelled as numbers. **b**, Fractional changes in population exposure to different landslide probability ranges (P) from 2000, 2050 and 2100. **c**, Changes in population exposure to landslides at the census tract level from 2000 to 2050, based on the mean value from eight ensemble member estimates. **d**, Fractional changes (%) in population exposure to landslides at the census tract level from 2000 to 2050. Basemaps in **c** and **d** created with MATLAB[28].

populated counties also demonstrate substantial increases in areal exposure to severe landslide, including Orange County (by 212.9 km^2, +25.6%), San Diego (by 924.6 km^2, +13.3%) and San Bernardino (by 2,910 km^2, +115.4%). Those increases are primarily contributed by substantially increased TC rainfall intensity, and partially influenced by the larger inter-model variations in TC landslide probability estimates from the SSP3-7.0 scenario, as shown in the interquartile range maps in Extended Data Fig. 5.

Population exposure to TC rainfall landslides

We overlay landslide probability maps from each GCM with population density estimates in 2000 and projections for 2050 and 2100 (SSP3, regional rivalry; Methods)[39]. A total of 90% of counties exhibit increases in ensemble mean population exposure to landslides from 2000 to 2050, with a median fractional increase of 72.1% across individual GCMs ranging from 36.1% to 410.6% (Fig. 4a). We also identify slight decreases in population exposure in 2100, albeit still mostly higher than the 2000 statistics, due to the projected decline in county-level population from 2050 to 2100 (Extended Data Fig. 6). Meanwhile, Los Angeles, San Diego and Orange County show large fractional increases in population exposed to severe landslide risk ($P > 0.8$, Fig. 4b). Census tracts with larger exposure (Extended Data Fig. 7) and more absolute change (Fig. 4c) are more likely to cluster over the mountainous areas along Los Angeles, Orange County and San Diego, while the fractional change map (Fig. 4d) shows a more complex and widespread spatial pattern.

Social equity has become a focus of debates on disaster exposure and vulnerability in both the USA and globally[40,41]. By integrating the current census-tract-level family income dataset with our estimates of future TC landslide probability (Methods), we show more low-income households (<US\$100,000 annual income) than high-income households (>US\$200,000 annual income) are exposed to landslides in both 2000 and 2050 (Extended Data Fig. 8). Low-income households (Fig. 5a) also face more increases in landslide exposure than high-income households from 2000 to 2050 (Fig. 5a,b), contributed by both spatial heterogeneity of household incomes and the changing landslide probability. The more detailed income breakdown analyses demonstrate stronger social disparities in projected changes in landslide exposure (Fig. 5a). The ensemble median exposure for <US\$50,000 annual income households will increase by 197%, while the >US\$200,000 annual income households will increase by only 40%. Number of households with >US\$200,000 income have larger net increases in exposure by ~86,500, which is 35% more than the net increase in exposure of

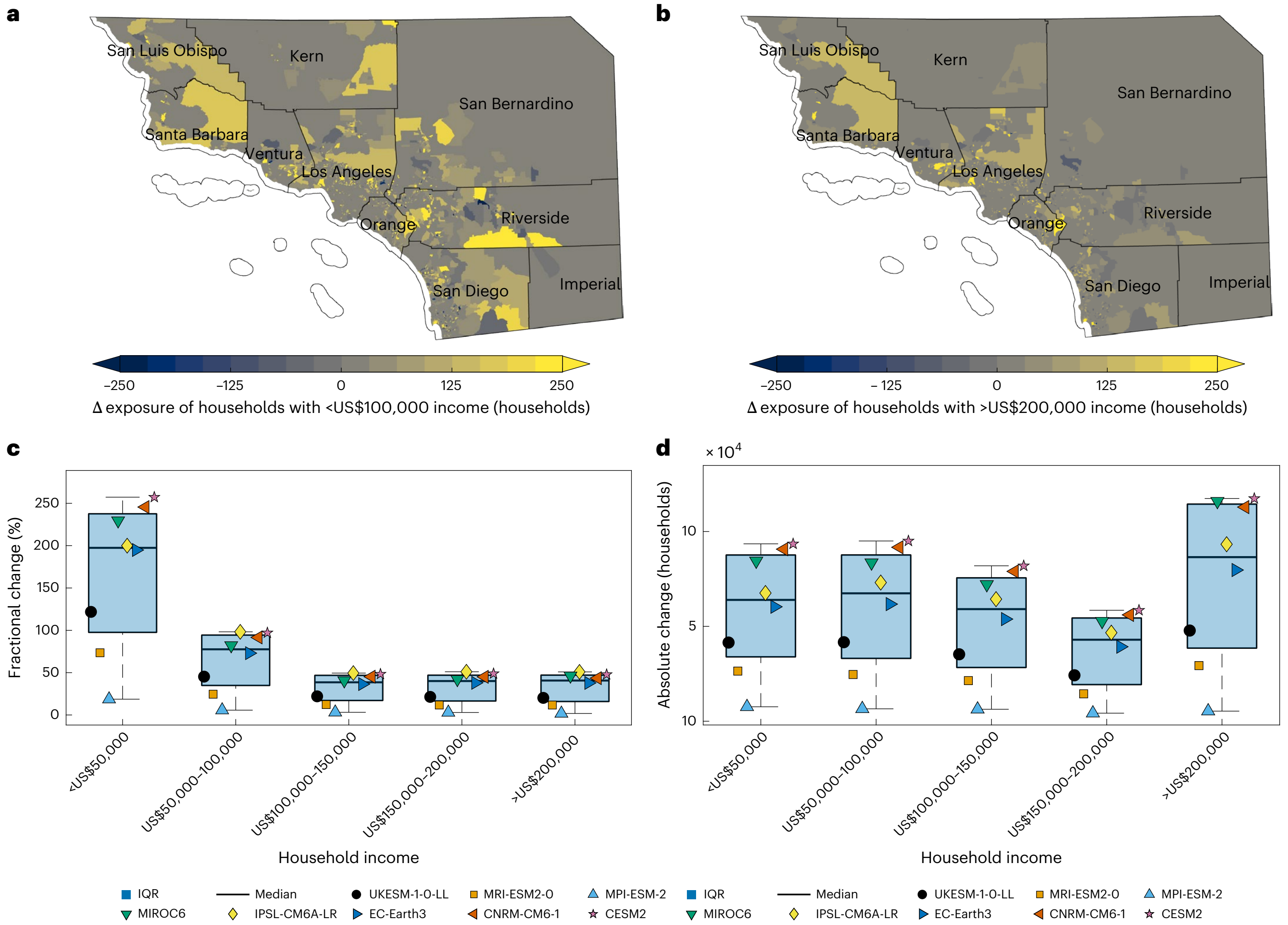

Fig. 5 | Changes in households exposed to landslides induced by TC rainfall events with a 100-year return period. **a**, Changes in households with <US$100,000 annual income exposed to landslide risk from the historical to the SSP3-7.0 scenario, mapped as the ensemble mean value by census tracts. **b**, Changes in households with >US$200,000 annual income exposed to landslide risk from the historical to the SSP3-7.0 scenario. **c**, Fractional changes in households exposed to landslides from the historical to the SSP3-7.0 scenarios, calculated as a lump sum across all census tracts for each GCM, shown as box-and-whisker plots for each household income category. The interquartile range (IQR, bounds defined as 25th and 75th percentiles) of eight GCM estimates (coloured dots) is shown as the height of the filled box, the median is the black line and the whiskers represent the minimum and maximums of the sample. **d**, Net changes in the number of households exposed to landslides from the historical to the SSP3-7.0 scenarios, shown as box-and-whisker plots for each household income category. Basemaps in **a** and **b** created with MATLAB[28].

households with <US$50,000 annual income (~63,900) but 34% less than the net increase in the exposure of households with <US$100,000 annual income (~131,000 when we combine the <US$50,000 and the US$50,000–100,000 income brackets). There is variability among GCM estimates (Fig. 5c,d), but they follow consistent patterns at different scales. Additionally, we overlay paid tax data at the zip code level with the same sets of landslide probability maps (Methods) and show that low-income households have larger fractional increases in exposed paid tax than high-income households (Extended Data Fig. 9 and Supplementary Fig. 16).

Discussion

Our results suggest a broad consensus on the increased TC rainfall risk under a warmer climate. The increased TC rainfall risk is very closely linked to substantial SST increases within the eastern Pacific TC development region (5–40° N, 140–80° W), as warmer SST is likely to be more favourable for TC development by providing larger surface enthalpy fluxes and releasing greater latent heat in the atmosphere[42,43], leading to higher rainfall rates. Under the SSP2-4.5 scenario, the regional SST also exhibits robust increasing trends (Supplementary Fig. 17), although the magnitudes are smaller than those under the SSP3-7.0 scenario. We also find increases in both specific and relative humidity over the eastern Pacific enhance TC rainfall rates following the Clausius–Clapeyron scaling, and even at a higher rate through 'super' Clausius–Clapeyron scaling at the local scale[32]. Note that there is uncertainty in the response of regional vertical wind shear to continued warming, with GCMs projecting slight increases in the future under SSP3-7.0 but observations showing decreases from 1979 to 2024[44]. Hence, its influence on the changing probability of TC landfall in Southern California requires further investigation.

There is pronounced spatial variability in TC rainfall across the region, as demonstrated by the return period maps of 100 mm TC rainfall (Extended Data Fig. 1), and the maps of TC rainfall with 100-year return periods (Extended Data Fig. 10; Supplementary Figs. 2b, 19 and 20) and 500-year return periods (Supplementary Figs. 18, 21 and 22). Larger TC rainfall is primarily concentrated in regions of complex terrain (Supplementary Fig. 14) facing the Pacific Ocean, possibly due to the rapid orographic lifting of moist air[10,24,45]. This effect can be captured by our TC rainfall algorithm using high-resolution topography data[46]. Our analyses also indicate that enhanced TC rainfall is introducing widespread increases in landslide risk across Southern California, with the most pronounced pattern over the coastal-facing mountain ranges. Some mountainous areas also have high population densities and are particularly susceptible to landslides when increasing TC rainfall and rapid urbanization effects are combined[47]. Southern California's population exposure to TC rainfall-induced landslides will likely increase rapidly from the present to 2050, driven by both the elevated probability of extreme TC rainfall under a warmer climate and projected population growth in the SSP3 scenario. However, a reduction in exposure will likely occur from 2050 to 2100, primarily due to SSP3's projected decline in total population in the latter half of the century[48].

The projected increases in TC rainfall and the associated landslide risk have implications for the public and decision-makers. In the current climate, atmospheric rivers during cool, wet seasons are typically regarded as the main drivers of rainfall in this region, and residents are generally well-adapted to these events. In contrast, heavy TC rainfall occurs less frequently but is usually more intense within a shorter period[49]. Furthermore, the climatological eastern Pacific TC season primarily overlaps with California's warm, dry seasons, potentially compounding the impacts of extreme drought and wildfires. Wildfires and long-lasting drought could also exacerbate flash floods and landslides in the region[50,51]. With more intense and frequent wildfires in California in recent decades[52], future research should investigate the hydroclimatic 'whiplash' effects on vegetation dynamics and incorporate these processes into landslide risk assessments[53,54].

The present study provides a county-level risk assessment of TC rainfall and associated landslides in Southern California, offering a basis for informing efforts to reduce hazard impacts that could be exacerbated by climate change, economic development and population growth. Mitigation strategies should include improving the prediction and monitoring of TC development over the Northeast Pacific, implementing stricter zoning regulations to restrict construction in areas with high landslide probability, maintaining robust vegetation to stabilize susceptible soils, and employing structural hardening measures to reinforce infrastructure in vulnerable zones. We also estimate the varied exposures to projected changes in TC rainfall-induced landslide risk among families with different annual incomes and tax brackets in Southern California. Low-income households (<US$50,000 annually) have disproportionately larger fractional increases in exposure to landslide risk than higher-income households (>US$200,000 annually), and the exposed paid tax has the fastest-growing rate for low-income households, which could increase their vulnerability when facing exacerbated TC-induced landslide risk under a changing climate[6], given the relatively limited resources available to those disadvantaged communities. Disparities in exposure and vulnerability have been previously reported for various hazard types in Southern California, including wildfires, urban flooding and heatwaves[44,55,56]. The large and disproportionate increases in population exposure in our study can be attributed to more frequent and intense TC rainfall events under a warmer climate and the widespread geographical distribution of low-income communities. Meanwhile, communities with limited resources face more challenges in recovery, as reflected in previous catastrophes such as hurricanes Katrina and Harvey[57,58]. Potential actions to mitigate this vulnerability include implementing policies that promote resilient and low-cost housing, adopting participatory approaches to urban planning that ensure fairness and safety, providing education and training in hazard prevention and offering reasonable relocation assistance for areas at high risk.

Online content

Any methods, additional references, Nature Portfolio reporting summaries, source data, extended data, supplementary information, acknowledgements, peer review information; details of author contributions and competing interests; and statements of data and code availability are available at https://doi.org/10.1038/s41558-026-02633-w.

References

1. Geiger, T., Frieler, K. & Bresch, D. N. A global historical data set of tropical cyclone exposure (TCE-DAT). *Earth Syst. Sci. Data* **10**, 185–194 (2018).
2. Krichene, H. et al. The social costs of tropical cyclones. *Nat. Commun.* **14**, 7294 (2023).
3. Mendelsohn, R., Emanuel, K., Chonabayashi, S. & Bakkensen, L. The impact of climate change on global tropical cyclone damage. *Nat. Clim. Change* **2**, 205–209 (2012).
4. Emanuel, K. Global warming effects on U.S. hurricane damage. *Weather Clim. Soc.* **3**, 261–268 (2011).
5. Smith, A. B. U.S. billion-dollar weather and climate disasters, 1980 - present (NCEI Accession 0209268). *National Centers for Environmental Information* https://doi.org/10.25921/stkw-7w73 (2024).
6. Jacox, M. G., Edwards, C. A., Hazen, E. L. & Bograd, S. J. Coastal upwelling revisited: Ekman, Bakun, and improved upwelling indices for the U.S. west coast. *J. Geophys. Res. Oceans* **123**, 7332–7350 (2018).
7. Chenoweth, M. & Landsea, C. The San Diego hurricane of 2 October 1858. *Bull. Am. Meteorol. Soc.* **85**, 1689–1698 (2004).
8. 43 dead or missing in California gale; Los Angeles is hit by new storm as Sunday damage is put at $1,000,000. *The New York Times* (The Associated Press, 26 September 1939).
9. Reinhart, B. J. *Hurricane Hilary* EP092023 (National Hurricane Center, 2024).
10. Huang, X. & Swain, D. L. Climate change is increasing the risk of a California megaflood. *Sci. Adv.* **8**, eabq0995 (2022).
11. Ralph, F. M. et al. A scale to characterize the strength and impacts of atmospheric rivers. *Bull. Am. Meteorol. Soc.* **100**, 269–289 (2019).
12. Guzzetti, F., Peruccacci, S., Rossi, M. & Stark, C. P. The rainfall intensity–duration control of shallow landslides and debris flows: an update. *Landslides* **5**, 3–17 (2008).
13. Swain, D. L., Langenbrunner, B., Neelin, J. D. & Hall, A. Increasing precipitation volatility in twenty-first-century California. *Nat. Clim. Change* **8**, 427–433 (2018).
14. Lin, N. & Emanuel, K. Grey swan tropical cyclones. *Nat. Clim. Change* **6**, 106–111 (2016).
15. Thorne, K. M., MacDonald, G. M., Chavez, F. P., Ambrose, R. F. & Barnard, P. L. Significant challenges to the sustainability of the California coast considering climate change. *Proc. Natl Acad. Sci.* **121**, e2310077121 (2024).
16. Prein, A. F. et al. The future intensification of hourly precipitation extremes. *Nat. Clim. Change* **7**, 48–52 (2017).
17. Reed, K. A., Wehner, M. F. & Zarzycki, C. M. Attribution of 2020 hurricane season extreme rainfall to human-induced climate change. *Nat. Commun.* **13**, 1905 (2022).
18. Molnar, P., Fatichi, S., Gaál, L., Szolgay, J. & Burlando, P. Storm type effects on super Clausius–Clapeyron scaling of intense rainstorm properties with air temperature. *Hydrol. Earth Syst. Sci.* **19**, 1753–1766 (2015).
19. Metropolitan and micropolitan statistical area population totals and components of change: 2020-2025. *US Census Bureau* https://www.census.gov/data/tables/time-series/demo/popest/2020s-total-metro-and-micro-statistical-areas.html (2021).
20. Huang, X., Swain, D. L. & Hall, A. D. Future precipitation increase from very high resolution ensemble downscaling of extreme atmospheric river storms in California. *Sci. Adv.* **6**, eaba1323 (2020).
21. Houze, R. A. Jr. Orographic effects on precipitating clouds. *Rev. Geophys.* https://doi.org/10.1029/2011RG000365 (2012).
22. DeHart, J. C. & Houze, R. A. Orographic modification of precipitation processes in Hurricane Karl (2010). *Mon. Weather Rev.* **145**, 4171–4186 (2017).

23. Zhu, L. & Aguilera, P. Evaluating variations in tropical cyclone precipitation in eastern Mexico using machine learning techniques. *J. Geophys. Res. Atmos.* **126**, e2021JD034604 (2021).
24. Semnani, S. J., Han, Y., Bonfils, C. J. & White, J. A. Assessing the impact of climate change on rainfall-triggered landslides: a case study in California. *Landslides* **22**, 1707–1724 (2025).
25. Oakley, N. S. et al. Investigating the atmospheric conditions associated with impactful shallow landslides in California (USA). *Earth Interact.* **28**, e240003 (2024).
26. Stanley, T. A. et al. Building a landslide hazard indicator with machine learning and land surface models. *Environ. Modelling Softw.* **129**, 104692 (2020).
27. Li, D., Qi, Y., Zhou, T. & Zhang, W. Future changes of socioeconomic exposure to potential landslide hazards over mainland China. *Weather Clim. Extrem.* **46**, 100731 (2024).
28. MATLAB v.R2024a (MathWorks, 2024).
29. Zhu, L. & Wang, Y. Replication data for: Increasing tropical cyclone rainfall and landslide risk in Southern California. *Zenodo* https://doi.org/10.5281/zenodo.18962075 (2026).
30. IPCC *Climate Change 2022: Impacts, Adaptation and Vulnerability* (Pörtner, H.-O. et al.) (Cambridge Univ. Press, 2023).
31. Shiogama, H. et al. Important distinctiveness of SSP3–7.0 for use in impact assessments. *Nat. Clim. Change* **13**, 1276–1278 (2023).
32. Stansfield, A. M. & Reed, K. A. Global tropical cyclone precipitation scaling with sea surface temperature. *npj Clim. Atmos. Sci.* **6**, 60 (2023).
33. Tang, B. & Emanuel, K. A ventilation index for tropical cyclones. *Bull. Am. Meteorol. Soc.* **93**, 1901–1912 (2012).
34. Chand, S. S. et al. Declining tropical cyclone frequency under global warming. *Nat. Clim. Change* **12**, 655–661 (2022).
35. Wang, Y., Rao, Y., Tan, Z.-M. & Schönemann, D. A statistical analysis of the effects of vertical wind shear on tropical cyclone intensity change over the western North Pacific. *Mon. Weather Rev.* **143**, 3434–3453 (2015).
36. Qin, L. et al. Global expansion of tropical cyclone precipitation footprint. *Nat. Commun.* **15**, 4824 (2024).
37. Wingo, M. T. & Cecil, D. J. Effects of vertical wind shear on tropical cyclone precipitation. *Mon. Weather Rev.* **138**, 645–662 (2010).
38. Stanley, T. A., Sutton, J. R. P., Vershel, R. S. & Amatya, P. M. Better satellite precipitation algorithms slightly improved landslide hazard assessment. *J. Appl. Meterol. Climatol.* **64**, 1379–1394 (2025).
39. Jones, B. & O'Neill, B. C. Spatially explicit global population scenarios consistent with the Shared Socioeconomic Pathways. *Environ. Res. Lett.* **11**, 084003 (2016).
40. Cutter, S. L., Boruff, B. J. & Shirley, W. L. Social vulnerability to environmental hazards. *Soc. Sci. Q.* **84**, 242–261 (2003).
41. Sanders, B. F. et al. Large and inequitable flood risks in Los Angeles, California. *Nat. Sustain.* **6**, 47–57 (2023).
42. Emanuel, K. Increasing destructiveness of tropical cyclones over the past 30 years. *Nature* **436**, 686–688 (2005).
43. Knutson, T. et al. Tropical cyclones and climate change assessment: part II: projected response to anthropogenic warming. *Bull. Am. Meteorol. Soc.* **101**, E303–E322 (2020).
44. Yin, Y., He, L., Wennberg, P. O. & Frankenberg, C. Unequal exposure to heatwaves in Los Angeles: impact of uneven green spaces. *Sci. Adv.* **9**, eade8501 (2023).
45. Zhang, W., Villarini, G., Vecchi, G. A. & Smith, J. A. Urbanization exacerbated the rainfall and flooding caused by hurricane Harvey in Houston. *Nature* **563**, 384–388 (2018).
46. Emanuel, K. Cyclone Jasper's rains in the context of climate change. *Proc. Natl Acad. Sci.* **121**, e2400292121 (2024).
47. Johnston, E. C. et al. Quantifying the effect of precipitation on landslide hazard in urbanized and non-urbanized areas. *Geophys. Res. Lett.* **48**, e2021GL094038 (2021).
48. Jiang, L., O'Neill, B. C., Zoraghein, H. & Dahlke, S. Population scenarios for U.S. states consistent with shared socioeconomic pathways. *Environ. Res. Lett.* **15**, 094097 (2020).
49. Allan, R. P. & Soden, B. J. Atmospheric warming and the amplification of precipitation extremes. *Science* **321**, 1481–1484 (2008).
50. Montgomery, D. R., Schmidt, K. M., Greenberg, H. M. & Dietrich, W. E. Forest clearing and regional landsliding. *Geology* **28**, 311–314 (2000).
51. Rengers, F. K. et al. Landslides after wildfire: initiation, magnitude, and mobility. *Landslides* **17**, 2631–2641 (2020).
52. Brown, P. T. et al. Climate warming increases extreme daily wildfire growth risk in California. *Nature* **621**, 760–766 (2023).
53. Swain, D. L. et al. Hydroclimate volatility on a warming Earth. *Nat. Rev. Earth Environ.* **6**, 35–50 (2025).
54. Swain, D. L. et al. Increasing hydroclimatic whiplash can amplify wildfire risk in a warming climate. *Global Change Biol.* **31**, e70075 (2025).
55. Casey, J. A. et al. Measuring long-term exposure to wildfire PM2.5 in California: time-varying inequities in environmental burden. *Proc. Natl Acad. Sci.* **121**, e2306729121 (2024).
56. Xie, W. & Meng, Q. Social vulnerability analysis of planned power outages: a spatial study of power outage in California caused by wildfire risk. *Sustain. Cities Soc.* **120**, 106163 (2025).
57. Fussell, E. & Harris, E. Homeownership and housing displacement after Hurricane Katrina among low-income African-American mothers in New Orleans. *Soc. Sci. Q.* **95**, 1086–1100 (2014).
58. Ma, C. & Culhane, D. P. Addressing low-income household sheltering needs after a disaster: a needs assessment among Hurricane Harvey housing victims. *Hous. Stud.* **39**, 1887–1902 (2024).

Methods

The synthetic TC model and risk assessment

We first downscale synthetic TCs based on eight CMIP6 GCMs (Supplementary Table 1) and the ERA5 reanalysis. We then generate 1,200 tracks for each CMIP6 model for two periods: 1985–2014 from the historical simulations and 2071–2100 from the socioeconomic pathway SSP3-7.0 simulations, which include a 7 W m^{-2} radiative forcing by the year 2100. Additionally, we generate 1,260 tracks based on the ERA5 reanalysis from 1980 to 2022. All CMIP6 (historical and SSP3-7.0) and ERA5 TCs are within 500 km of Los Angeles (34° 03′ N, 118° 15′ W) with a maximum one-minute surface wind ≥35 knots (65 km h^{-1}). Here we assume that the annual frequency of TCs does not change (~0.11 for TCs within 500 km of Los Angeles) but follows a Poisson distribution, based on the default setup of a synthetic TC downscaling algorithm[59]. We apply the TC rainfall algorithm[60–63], which can simulate hourly rain rates at any location from a rain field defined by each TC location along each synthetic TC track. This algorithm has been validated using in situ and remotely sensed precipitation products[61,63]. The TC rainfall algorithm calculates TC convective rainfall based on quasi-balanced physics, with additional considerations for the surrounding atmospheric environment, surface roughness and topographic information derived from a high-resolution digital elevation model at 0.1° (ref. 46). The hourly rain rate P_{rate} can be generally written as equation (1):

$$P_{\mathrm{rate}} = \epsilon_{\mathrm{p}} \frac{\rho_{\mathrm{air}}}{\rho_{\mathrm{liquid}}} q_{\mathrm{s}} w \tag{1}$$

where ϵ_{p} is precipitation efficiency set to 0.5 (ref. 64), ρ_{air} and ρ_{liquid} are the water vapour and liquid water density, respectively (the ratio is set to 0.0012), q_{s} is the saturation specific humidity and w is the vertical velocity, which is controlled by the TC wind field, the surface roughness from topography, TC vortex stretching and the contribution from the baroclinic shear (more details can be found in ref. 62).

Then, we calculate and collect hourly rain rates at all 1-km grids across Southern California for each TC event, and aggregate them to obtain the cumulative rainfall for each TC event (96 hours). We construct a climatology of TC event rainfall based on 1,200 TCs per GCM or ERA5 run. From the full set of 394 × 877 1-km grids, we used a land mask to subset the dataset to 199,728 land-only grids.

Previous studies[61,63,65] used an empirical approach to estimate the probability density functions and return periods for different TC rainfall algorithm magnitudes. In this study, we employ a different approach to fit the tails of the TC event rainfall data using a GPD, based on the extreme value theory[66]. The probability density function of GPD is given in equation (2):

$$f(x \mid k, \sigma, \theta) = \left(\frac{1}{\sigma}\right)\left(1 + k\frac{(x-\theta)}{\sigma}\right)^{-1-\frac{1}{k}} \tag{2}$$

where k is the shape parameter ($k \neq 0$), σ is the scale parameter and θ is the threshold parameter. If $k = 0$ and $\theta = 0$, the GPD is equivalent to the exponential distribution. If $k > 0$ and $\theta = \sigma/k$, the GPD is equivalent to the Pareto distribution with a scale parameter equal to σ/k and a shape parameter equal to $1/k$. The cumulative distribution function is then given in equation (3):

$$F(x \mid k, \sigma, \theta) = \begin{cases} 1 - \left(1 + k\frac{(x-\theta)}{\sigma}\right)^{-\frac{1}{k}} & \text{for } k \neq 0 \\ 1 - \exp\left(-\frac{(x-\theta)}{\sigma}\right) & \text{for } k = 0 \end{cases} \tag{3}$$

Finally, the return period is calculated as equation (4):

$$\text{Return period} = \frac{1}{1 - F(x \mid k, \sigma, \theta)} \times \text{scale} \tag{4}$$

where F is the cumulative distribution function calculated from equation (3), and we set the scale factor to 10, as we only model TC event rainfall with a return period greater than 10 years. We set 100 steps, evenly distributed within each TC rainfall sample range, to estimate the return period curves, then create 1,000 bootstrap samples for each step using the Monte Carlo algorithm to fit the GPD across the full range. We also use bootstrapped samples at each step to estimate 95% confidence intervals for the upper and lower bounds. Then, the mean, upper and lower uncertainty boundaries of the GPD are transformed into return periods for specific TC rainfall magnitudes. We then repeat this algorithm for all 1-km grids over land and create their TC rainfall risk curves for ERA5 and all individual ensemble members from both the historical and the SSP3-7.0 scenarios. We can estimate the corresponding TC rainfall magnitude from given return intervals (for example, 100 years) or, conversely, estimate the return interval based on the given TC rainfall magnitude (for example, 100 mm). These estimations apply spline interpolation between granular steps based on each risk curve. We can finally map TC rainfall risk (return period for a given magnitude or magnitude for a given return period) across Southern California with high spatial resolution (1 km). We use an official definition[67] of the eastern Pacific basin of TCs as the spatial extent (5–40° N, 140–80° W) to analyse the monthly variability in SST, 500 hPa specific humidity and vertical wind shear from the ERA5 reanalysis and each GCM, since these are important environmental conditions for determining TC development and characteristics.

Landslide modelling

We sample 20 out of 1,200 events from each GCM downscaling set based on the accumulative TC rainfall with a 100-year return period at Los Angeles. We obtain the 100-year TC rainfall amount from the risk curve for Los Angeles via spline interpolation, then select 20 events with the 100-year TC rainfall amount as the median. We then record hourly TC rain rates for 96 hours for each of these 20 events at 1-km grid resolution and extract the 72-hour window of daily rain rates with the largest total rainfall (the first 48 hours for antecedent rainfall and the last 24 hours for the triggering day). These rain rates from each TC event are then coupled with the LHASA model to estimate daily landslide probabilities at 1-km resolution. LHASA 2.1, developed by the National Aeronautics and Space Administration, is a hybrid landslide hazard model driven by real-time rain rate measurements from the Global Precipitation Measurement Mission. It uses a machine learning-based probabilistic prediction approach, combining static and dynamic variables, to provide global, real-time, high-resolution landslide probability estimates[68,69]. We use the same initial condition (constant surface conditions and vegetation, soil moisture observed on 21 August 2023) for Hurricane Hilary in LHASA simulations of all TC events from both the historical and SSP3-7.0 scenarios for consistency.

In total, we simulate 160 (20 × 8) TC events for each scenario ensemble. Then we compute the maximum daily landslide probability over the three-day LHASA simulation window for each grid and event, and calculate the median across 20 events for each GCM downscaling run. Finally, we calculate the ensemble median across all GCMs within the historical and SSP3-7.0 ensembles for comparison and change detection. Therefore, projections of changes in landslide probability are primarily based on the changes in TC rainfall and its interactions with the orography. Uncertainty in change detection and attribution could be partially attributed to variations in the spatial pattern of individual TC rainfall events; however, we choose 20 events for each set to minimize this uncertainty. Recording larger sets of events is also limited by data storage capacity. We then aggregate the results by county and create maps that describe the spatial variations in changes in landslide probability from the historical ensemble to the SSP3-7.0 ensemble. The detailed 1-km landslide maps are directly transferred to the next population exposure and disparity analysis. The LHASA model is one of the currently available state-of-the-science landslide prediction models. However, it still needs further calibration using more complete samples of both landslide and non-landslide observations.

Population exposure to landslides and social disparity

We obtain population data[48] from spatially explicit global population scenarios consistent with the SSPs and merge them with our estimates of landslide risk. This population projection was developed from a gravity-based downscaling model. It is quantitatively consistent with the best available census data and urbanization projections based on SSPs and qualitatively consistent with the assumptions of SSP narratives on spatial development[39]. The original population projection has a spatial resolution of 1/8 arc, which is further downscaled to a 1-km resolution and shared by the Socioeconomic Data and Applications Center at Columbia University[70]. We select the population projection from the SSP3 ('regional rivalry') scenario to match the SSP3-7.0 scenario used for the TC downscaling.

We first combine the Southern California population estimate in 2000 with the historical landslide estimates (1985–2014), thereby constituting a baseline historical population exposure to landslide risk. The population exposure in 2000 is calculated as the 2000 population × the historical landslide probability at each 1-km grid. We also calculate population exposures for 2050 and 2100 under the SSP3 scenario as follows: 2050 population × SSP3-7.0 landslide probability and 2100 population × SSP3-7.0 landslide probability, respectively. We summarize high-resolution estimates of population exposure and their ratios within geopolitical boundaries (counties, census tracts and zip codes), then link the population exposure ratio (defined as the exposed population divided by the total population) to income and tax data to analyse social disparities in the final step.

Households with different annual incomes may differ in their exposure to natural hazards and their ability to recover[71], so we use household income data at the census tract level from the US Census in 2023[72] to study social disparities in TC rainfall-induced landslide risk. We first calculate the number of households exposed to the TC landslide in each census tract as follows: the total number of households × population exposure ratio. We reclassified the original ten income brackets into five classes with equal intervals for simplicity in discussing the results. Then, we estimate the number of households exposed in each reclassified income bracket as follows: the total number of households exposed in the TC landslide in each census tract × the fraction of households in each income bracket. We then summarize and map the exposure of households across income groups and their changes from the historical scenario to the SSP3-7.0 scenario, showing both the ensemble mean and inter-GCM variability. Here we assume that the number of families with different annual income ranges remains constant within each census tract between 2000 and 2100, and that the number of households is proportional to the population size. Only the TC landslide probability change, the population change and their combination with the static spatial variations in family income determine the changes in exposure. To support our findings, we also obtain the 2022 tax bracket data from the US Internal Revenue Service[73] and complete the same set of calculations to estimate the household's paid tax exposure to the landslide. We adapt colour-blind-safe palettes for all our maps and figures[74].

Data availability

All curated data used for the figures and results in the paper are available via Zenodo at https://doi.org/10.5281/zenodo.18962075 (ref. 29), under a single zipped folder named 'Codes+AndData_NCLIM-25051495A.zip'. TC track data can be made available from co-author K.E. under a non-commercial, non-distribution agreement. The data used for the LHASA landslide model can be accessed from the official website at https://github.com/nasa/LHASA. The income and tax bracket data are also freely available via https://data.census.gov/map and https://www.irs.gov/statistics/soi-tax-stats-individual-income-tax-statistics-zip-code-data-soi.

Code availability

Codes for TC rainfall are in the zipped folder 'MIT_TCR_scripts_ver6.7.zip', and codes to replicate all figures are in the zipped folders 'CodesAndData_NCLIM-25051495A.zip' and 'Codes_NCLIM-25051495A_v2.zip'; both are available via Zenodo at https://doi.org/10.5281/zenodo.18962075 (ref. 29). The source codes for the LHASA 2.1 landslide model are also freely available from https://github.com/nasa/LHASA.

References

59. Emanuel, K. Response of global tropical cyclone activity to increasing CO_2: results from downscaling CMIP6 models. *J. Clim.* **34**, 57–70 (2021).
60. Emanuel, K. Assessing the present and future probability of Hurricane Harvey's rainfall. *Proc. Natl Acad. Sci.* **114**, 12681–12684 (2017).
61. Feldmann, M., Emanuel, K., Zhu, L. & Lohmann, U. Estimation of Atlantic tropical cyclone rainfall frequency in the United States. *J. Appl. Meterol. Climatol.* **58**, 1853–1866 (2019).
62. Lu, P., Lin, N., Emanuel, K., Chavas, D. & Smith, J. Assessing hurricane rainfall mechanisms using a physics-based model: Hurricanes Isabel (2003) and Irene (2011). *J. Atmos. Sci.* **75**, 2337–2358 (2018).
63. Zhu, L., Quiring, S. M. & Emanuel, K. A. Estimating tropical cyclone precipitation risk in Texas. *Geophys. Res. Lett.* **40**, 6225–6230 (2013).
64. Meiler, S. et al. Navigating and attributing uncertainty in future tropical cyclone risk estimates. *Sci. Adv.* **11**, eadn4607 (2025).
65. Zhu, L., Emanuel, K. & Quiring, S. M. Elevated risk of tropical cyclone precipitation and pluvial flood in Houston under global warming. *Environ. Res. Lett.* **16**, 094030 (2021).
66. Embrechts, P., Mikosch, T. & Klüppelberg, C. *Modelling Extremal Events: For Insurance and Finance* (Springer-Verlag, 1997).
67. Glossary of NHC Terms. *National Hurricane Center* https://www.nhc.noaa.gov/aboutgloss.shtml (2025).
68. Stanley, T. A. et al. Data-driven landslide nowcasting at the global scale. *Front. Earth Sci.* https://doi.org/10.3389/feart.2021.640043 (2021).
69. Khan, S., Kirschbaum, D. B., Stanley, T. A., Amatya, P. M. & Emberson, R. A. Global landslide forecasting system for hazard assessment and situational awareness. *Front. Earth Sci.* https://doi.org/10.3389/feart.2022.878996 (2022).
70. Gao, J. Global 1-km downscaled population base year and projection grids based on the Shared Socioeconomic Pathways, revision 01. *NASA Socioeconomic Data and Applications Center (SEDAC)* https://doi.org/10.7927/q7z9-9r69 (2017).
71. Rentschler, J., Salhab, M. & Jafino, B. A. Flood exposure and poverty in 188 countries. *Nat. Commun.* **13**, 3527 (2022).
72. American community survey: income in the past 12 months (in 2023 inflation adjusted dollars). *US Census Bureau* https://data.census.gov/all (2023).
73. SOI Tax Stats: individual income tax statistics – ZIP Code data (SOI). *Internal Revenue Service* https://www.irs.gov/statistics/soi-tax-stats-individual-income-tax-statistics-zip-code-data-soi (2025).
74. Crameri, F., Shephard, G. E. & Heron, P. J. The misuse of colour in science communication. *Nat. Commun.* **11**, 5444 (2020).

Acknowledgements

L.Z. acknowledges funding support from NSF (no. 7037930). Y.W. acknowledges funding support from NSF (no. 2440581). K.E.'s contribution was part of the MIT Climate Grand Challenge on Weather and Climate Extremes, supported by Schmidt Sciences. Y.W., S.N.T. and N.S.D. acknowledge support from Stanford Doerr School of Sustainability.

Author contributions

Conceptualization: Y.W., L.Z., K.E. Methodology: L.Z., Y.W., K.E. Data analysis: L.Z., Y.W., S.N.T. Visualization: L.Z., Y.W., N.S.D. Writing—original draft: L.Z., Y.W. Writing—review and editing: Y.W., L.Z., K.E., S.N.T., N.S.D.

Competing interests

The authors declare no competing interests.

Additional information

Extended data is available for this paper at https://doi.org/10.1038/s41558-026-02633-w.

Supplementary information The online version contains supplementary material available at https://doi.org/10.1038/s41558-026-02633-w.

Correspondence and requests for materials should be addressed to Yuan Wang.

Peer review information *Nature Climate Change* thanks Jorge Luis García Franco, Dalia Kirschbaum, Chenyi Ma and the other, anonymous, reviewer(s) for their contribution to the peer review of this work.

https://doi.org/10.1038/s41558-026-02633-w

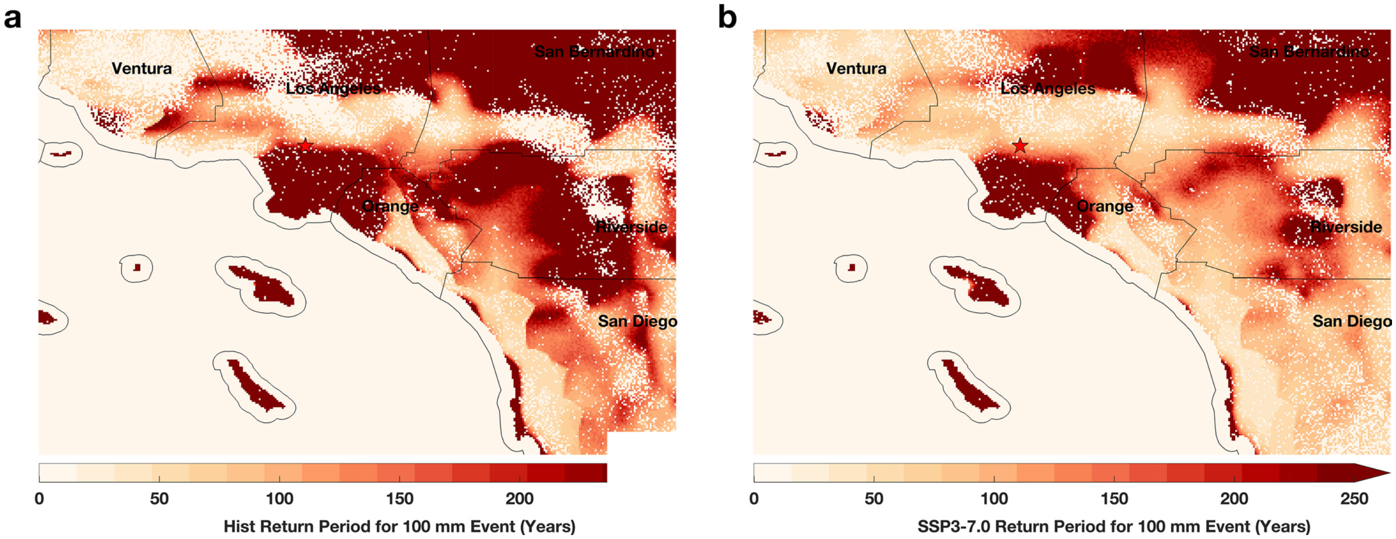

Extended Data Fig. 1 | Return periods for 100 mm TC rainfall event at different locations. a. the historical ensemble means; **b**. the SSP 3–7.0 ensemble mean. The return period at each location is calculated as the mean of the return period estimates from eight GCMs. Basemaps in **a** and **b** created with MATLAB[28].

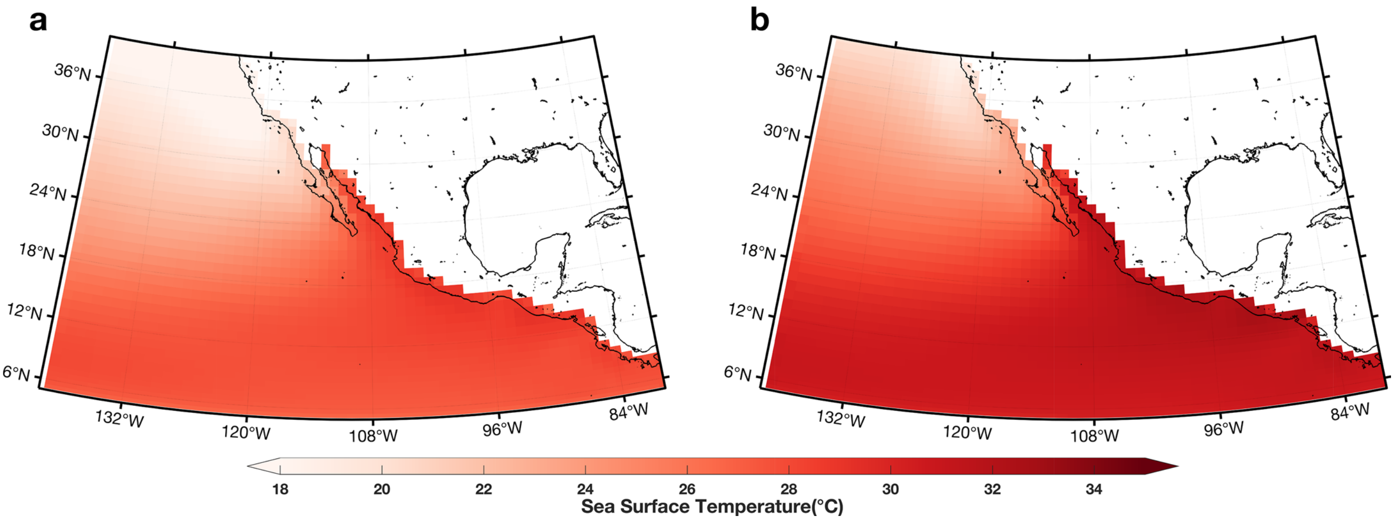

Extended Data Fig. 2 | Spatial distribution of the monthly mean Sea Surface Temperature. a. the Hist ensemble (1985–2014) and **b**. SSP3-7.0 ensemble (2071–2100) from eight GCMs (different GCM spatial grids are linearly rescaled into the same spatial grids based on UKESM1–0-LL). Basemaps in **a** and **b** created with MATLAB[28].

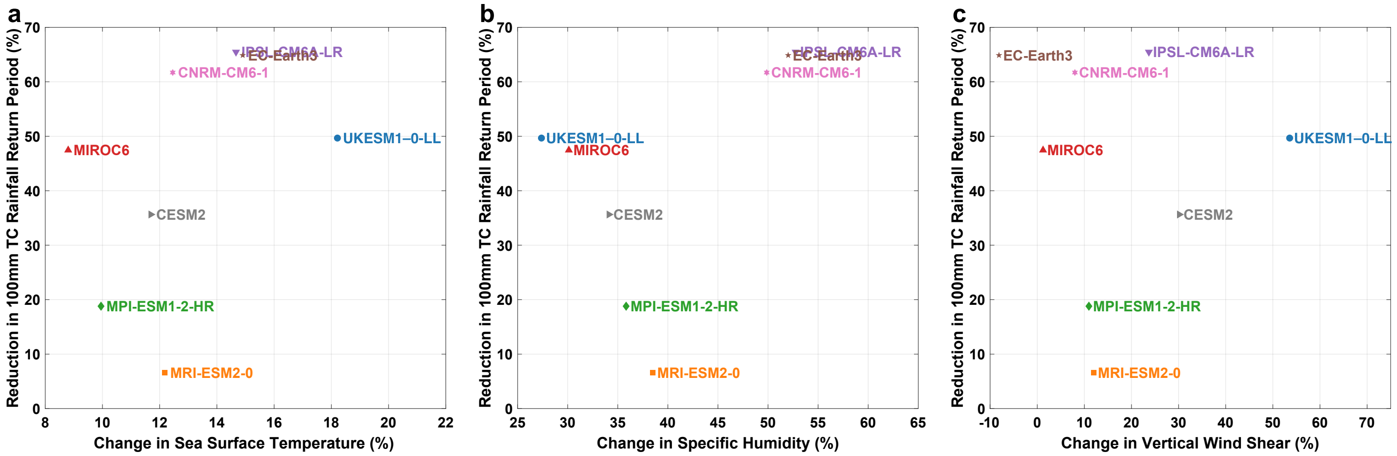

Extended Data Fig. 3 | Sensitivity of the return period of 100 mm TC rainfall to changes in environmental forcings from Hist (1985–2014) to SSP3–7.0 (2071–2100) for each of eight GCMs. a. Sea Surface Temperature; **b**. Specific Humidity; **c**. Vertical Wind Shear.

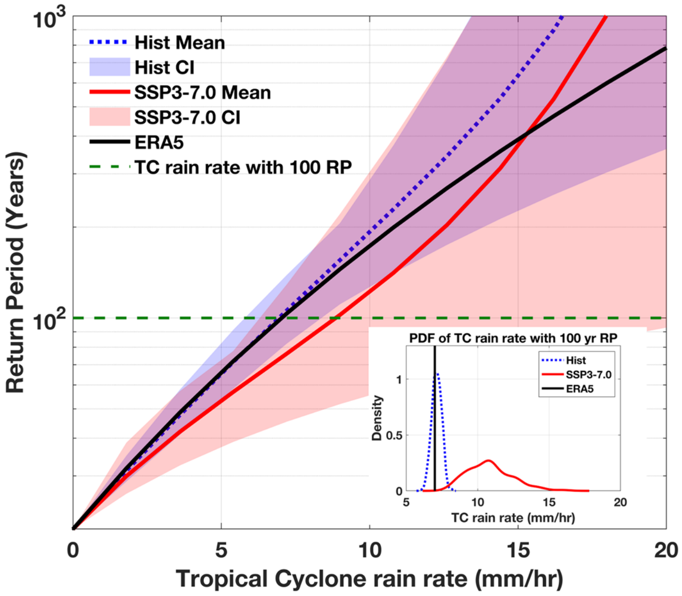

Extended Data Fig. 4 | Tropical Cyclone hourly rain rate and its return periods based on the historical (Hist), SSP3-7.0 climate scenarios, and ERA5 reanalysis. Lines represent 8-model ensemble means for the historical runs (blue), SSP3-7.0 runs (red), and the ERA5 run (black) for Los Angeles (34°03′N, 118°15′W) and shadings represent upper and lower model estimates from the historical ensemble (blue) and SSP3-7.0 ensemble (red); the embedded sub-panel shows the probability distribution function (PDF) of TC rain rate with 100 year return period based on eight models of Hist (blue) and SSP3-7.0 climate scenarios (red), estimated by bootstrapping ensemble GCM estimates, and the ERA5 estimate (black straight line). The green dashed line in the main figure represents the 100-year return period for comparison.

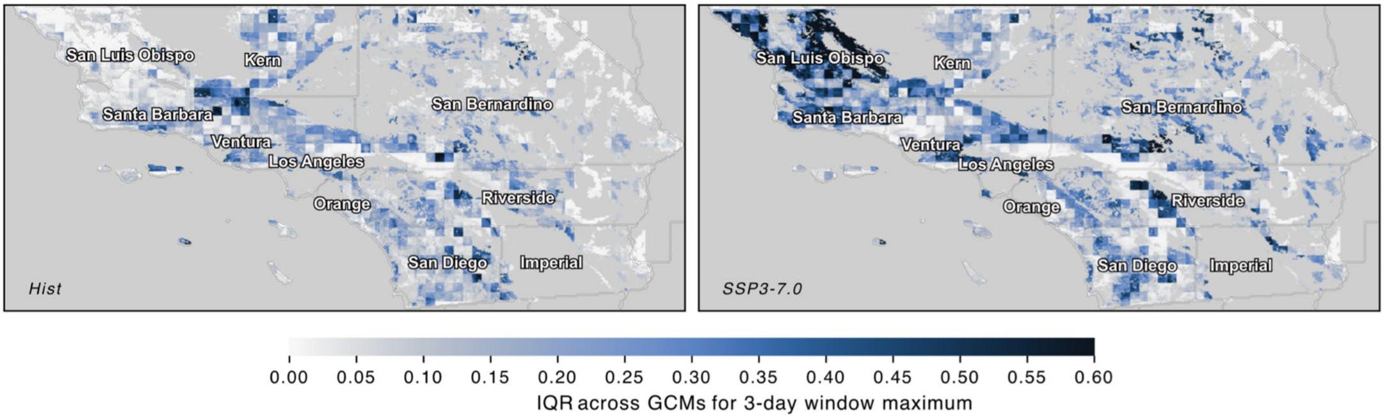

Extended Data Fig. 5 | The interquartile range (IQR) map for the median landslide probability across GCMs for the 3-day window maximum of the historical ensemble (Hist) and the SSP3-7.0 ensemble. Basemap administrative boundaries from GADM v. 3.6.

https://doi.org/10.1038/s41558-026-02633-w

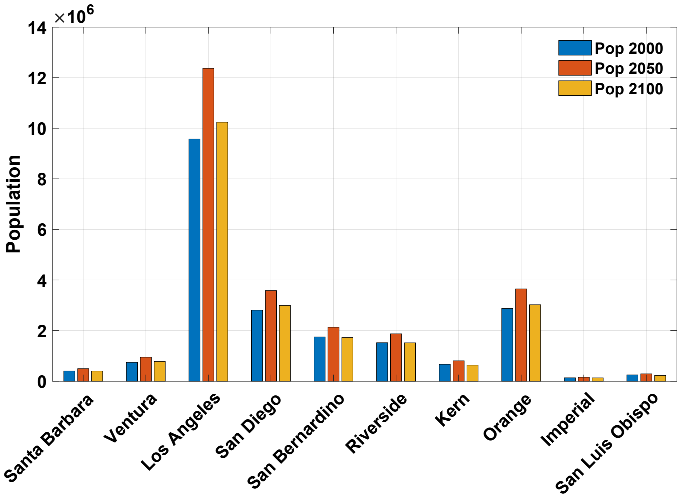

Extended Data Fig. 6 | The total population projection for each Southern California county by SSP3 in 2000, 2050, and 2100.

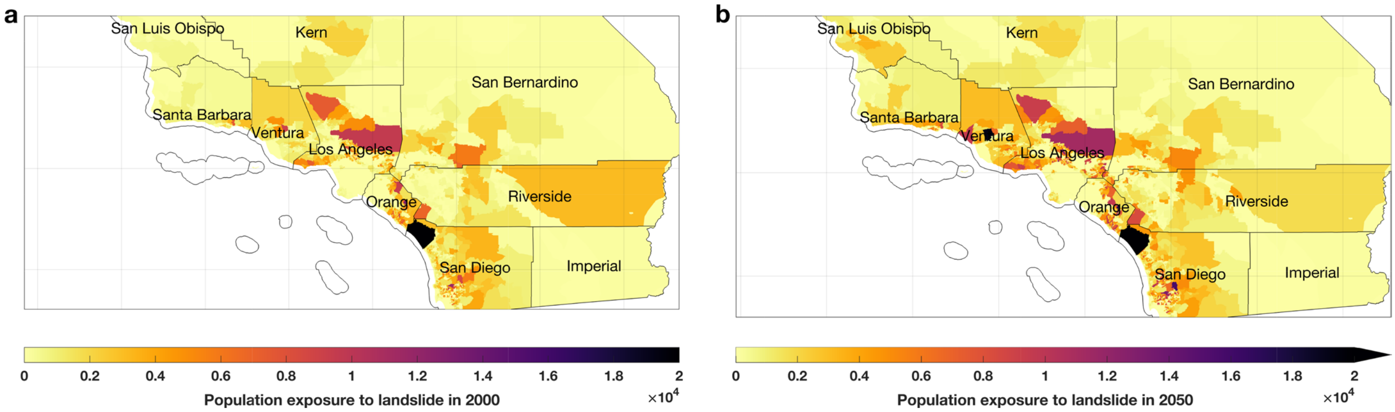

Extended Data Fig. 7 | Population exposure to landslides in 2000 and 2050. **a**. population exposure to landslides at the census tract level in 2000 based on the mean value from eight Hist ensemble member estimates, calculated from the Hist landslide probability and the SSP3 population estimation for 2000. **b**. projected exposure to landslides at the census tract level in 2050 based on the mean value from eight SSP3-7.0 ensemble member estimates, calculated from the SSP3-7.0 landslide probability and the SSP3 population projection for 2050. Basemaps created with MATLAB[28].

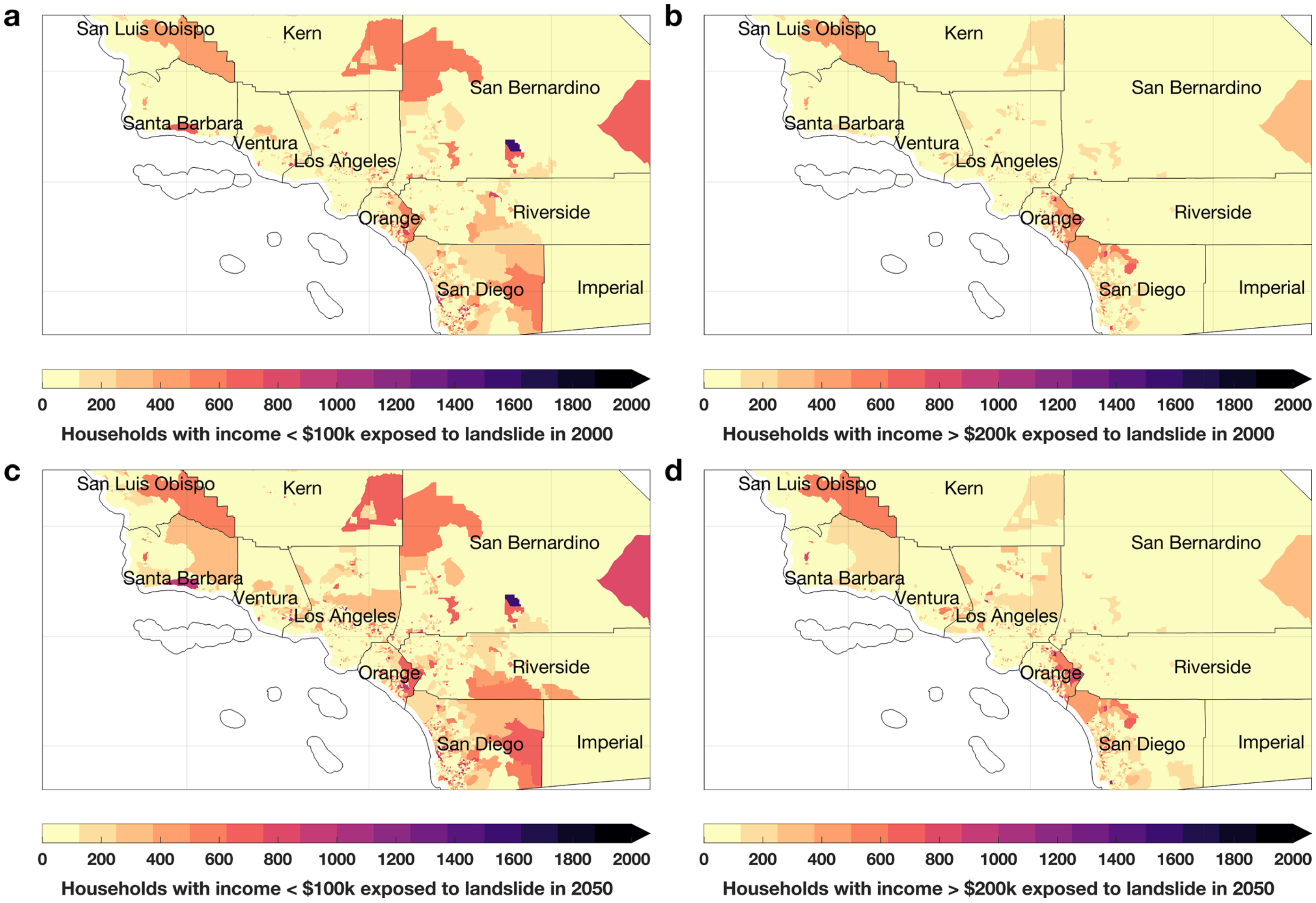

Extended Data Fig. 8 | Population exposure to landslides within census tracts summarized by income levels. a. number of households with < $100,000 ($100k) annual income exposed to landslides in the Hist scenario in 2000; **b**. number of households with > $200,000 ($200k) annual income exposed to landslides in the Hist scenario in 2000; **c**. number of households with < $100,000 ($100k) annual income exposed to landslides in the SSP3-7.0 scenario in 2050; **d**. number of households with > $200,000 ($200k) annual income exposed to landslides in the SSP3-7.0 scenario in 2050. We assume the fraction of household income does not change in each census tract from 2000 to 2050. Basemaps created with MATLAB[28].

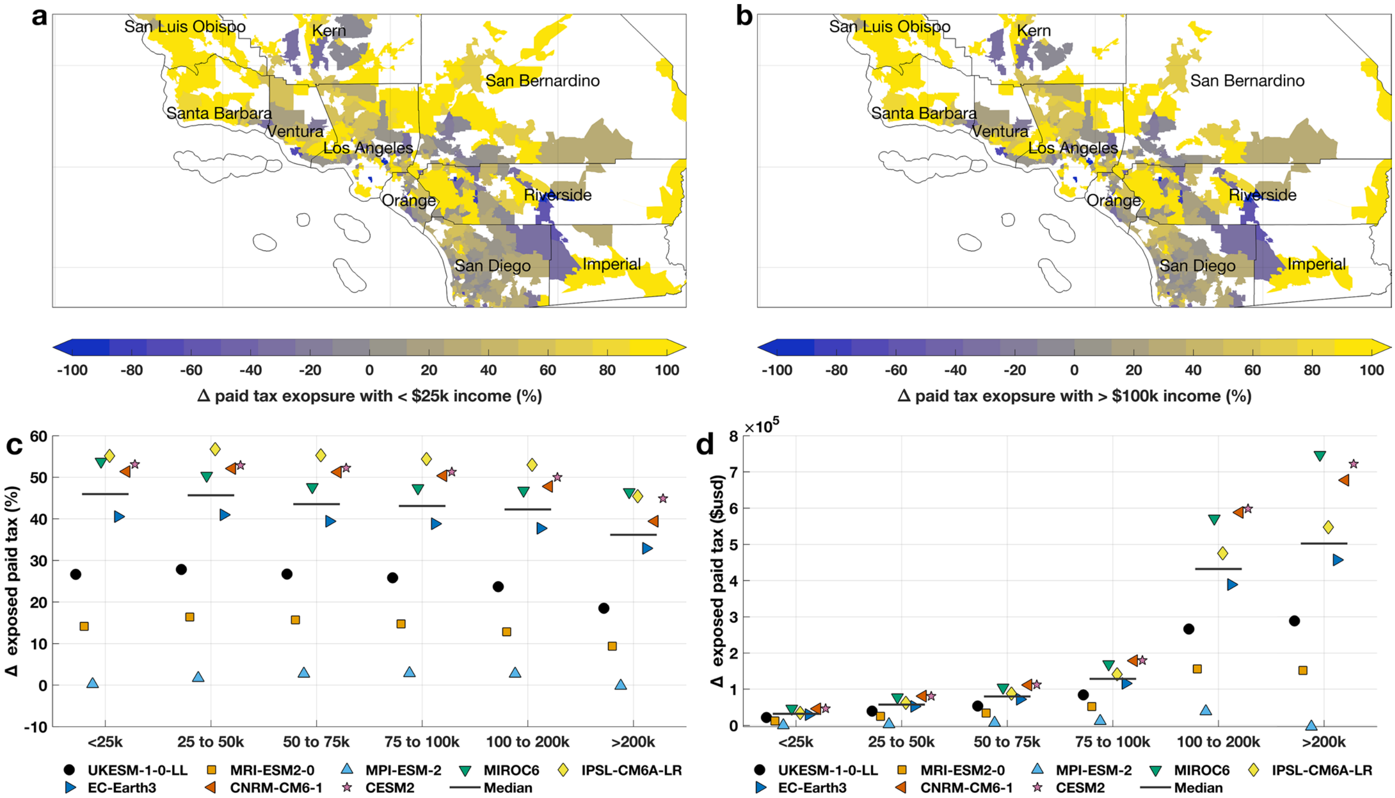

Extended Data Fig. 9 | The changes in paid tax exposure to landslide hazards. **a**. fractional (%) change in the paid tax exposure for households with < 25k annual income (first tax bracket) from Hist to SSP3-7.0, summarized within each zip code; **b**. fractional (%) change in the paid tax exposure for households with > 200k annual income (sixth tax bracket) from Hist to SSP3-7.0 summarized within each zip codes; **c**. census tract mean fractional changes of total paid tax exposure from Hist to SSP3-7.0, grouped by six tax brackets (income ranges), with distribution of separate GCM models and their median shown; **d**. census tract mean changes in total paid tax exposure ($ USD) from Hist to SSP3-7.0, grouped by six tax brackets (income ranges), with the distribution of separate GCM models and their median values shown. Basemaps in **a** and **b** created with MATLAB[28].

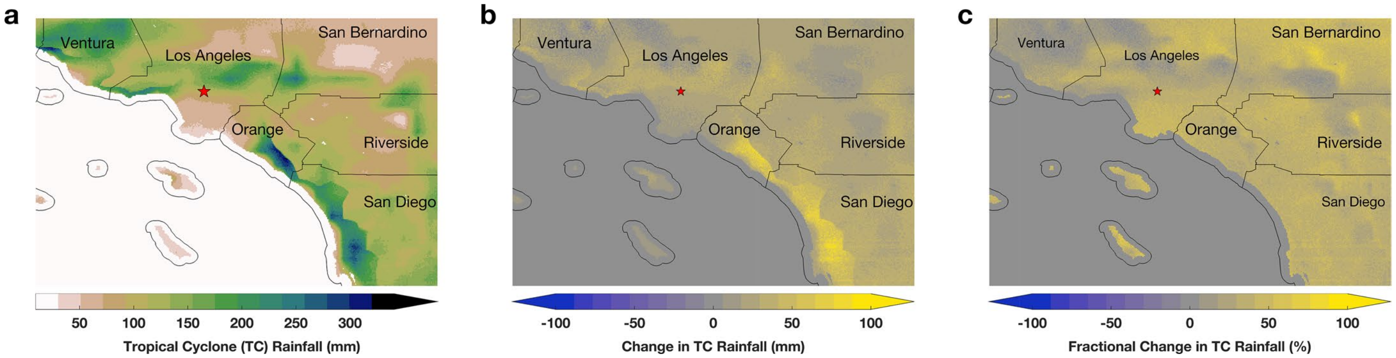

Extended Data Fig. 10 | Tropical cyclone rainfall and change based on 100-year return period. a. the spatial distribution of event TCP with a 100-year return period (100-year TCP) calculated as the ensemble mean of eight models from the SSP3-7.0 run; **b**. the absolute change of ensemble means of 100-year TCP from the historical (Hist) to SSP3-7.0, calculated as SSP3-7.0 - Hist; **c**. the fractional change of ensemble means of 100-year TCP from Hist to SSP3-7.0, calculated as (SSP3-7.0 - Hist)/Hist*100%. Basemaps created with MATLAB[28].